

FastSTAR: Spatiotemporal Token Pruning for Efficient Autoregressive Video Synthesis

Sungwoong Yune^{*✉}, Suheon Jeong^{*}, and Joo-Young Kim^(✉)

Korea Advanced Institute of Science and Technology
{imwooong, sh.jeong, jooyoung1203}@kaist.ac.kr



Fig. 1: FastSTAR achieves a 2.01 \times end-to-end speedup on a single H100 GPU for T2V and I2V tasks, maintaining high fidelity with PSNR of 28.29 and 25.65, respectively.

Abstract. Visual Autoregressive modeling (VAR) has emerged as a highly efficient alternative to diffusion-based frameworks, achieving comparable synthesis quality. However, as this paradigm extends to Space-time Autoregressive modeling (STAR) for video generation, scaling resolution and frame counts leads to a "token explosion" that creates a massive computational bottleneck in the final refinement stages. To address this, we propose **FastSTAR**, a training-free acceleration framework designed for high-quality video generation. Our core method, **Spatiotemporal Token Pruning**, identifies essential tokens by integrating two specialized terms: (1) *Spatial similarity*, which evaluates structural convergence across hierarchical scales to skip computations in regions where further refinement becomes redundant, and (2) *Temporal similarity*, which identifies active motion trajectories by assessing feature-level

^{*} Equal contribution

variations relative to the preceding clip. Combined with a **Partial Update** mechanism, FastSTAR ensures that only non-converged regions are refined, maintaining fluid motion while bypassing redundant computations. Experimental results on InfinityStar demonstrate that FastSTAR achieves up to a $2.01\times$ speedup with a PSNR of 28.29 and less than 1% performance degradation, proving a superior efficiency-quality trade-off for STAR-based video synthesis.

Keywords: Efficient Video Synthesis · Spacetime Autoregressive modeling · Training-free Acceleration · Token Pruning · Partial Update

1 Introduction

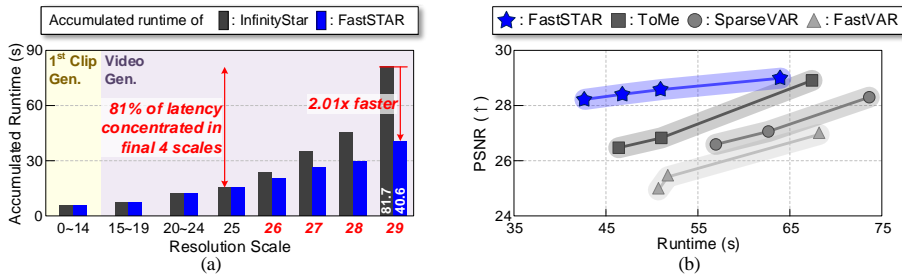


Fig. 2: (a) Latency breakdown for generating a 720p video (5s, 81 frames), comparing InfinityStar with FastSTAR. (b) Latency vs. PSNR trade-off curves for T2V synthesis. FastSTAR establishes the Pareto frontier, consistently surpassing existing baselines.

Visual Autoregressive modeling (VAR) [11, 31] has recently emerged as a powerful paradigm for visual generation, offering superior inference efficiency by redefining image synthesis as a coarse-to-fine next-scale prediction task. Unlike diffusion models [3–5, 27] that synthesize content through the iterative denoising of random noise [12, 23, 28], VAR-based frameworks progressively accumulate multi-scale residual feature maps. Building on this success, the recent Spacetime Autoregressive modeling (STAR) [22] utilizes a 3D-VAE [32] to tokenize video data into a spacetime pyramid, maintaining robust temporal consistency. However, the addition of the temporal dimension T escalates the computational complexity of the attention layer from $\mathcal{O}(H^2W^2)$ to $\mathcal{O}(T^2H^2W^2)$, where H and W denote the spatial resolution of the token map. Our profiling reveals that this quadratic growth manifests as a critical computational imbalance, where the last 4 out of the total resolution scales account for a disproportionate 81% of the total inference latency (Fig. 2(a)).

To address this "token explosion", existing reduction methods [1, 6, 10] suffer from distinct architectural limitations when applied to STAR. First, image-centric metric evaluations lead to the inaccurate identification of essential tokens, as they struggle to effectively detect the intricate temporal dynamics and motion trajectories inherent in video. Second, structural mismatches in token merging distort discrete feature distributions, triggering an error feedback loop that propagates across subsequent scales and spreads spatially as resolution increases. To

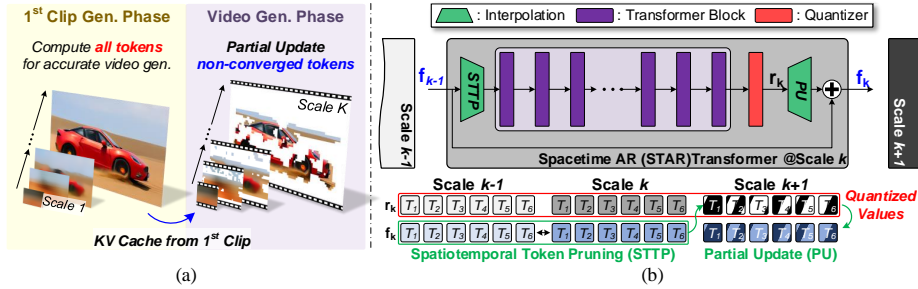


Fig. 3: (a) Overview of the FastSTAR framework. (b) Overall Mechanism of FastSTAR; Spatiotemporal Token Pruning identifies converged regions to completely skip transformer blocks, while Partial Update preserves structural integrity.

overcome these challenges, scale-wise spectral analysis (§ 3.2) demonstrates that while low-frequency global structures stabilize in the early stages, high-frequency details necessitate continuous updates until the final scale.

To leverage these insights, we propose **FastSTAR**, a training-free acceleration framework specifically tailored for high-quality video synthesis (Fig. 3). Unlike conventional token merging [1, 20] or cached-token restoration [17] that often distort latent representations and degrade visual fidelity in the VAR paradigm, FastSTAR adopts a pruning-over-merging strategy to preserve structural integrity. Our framework consists of two core components:

- **Spatiotemporal Token Pruning (STTP):** It identifies non-converged tokens by integrating spatial and temporal similarity. The spatial term evaluates structural convergence across scales, while the temporal term captures motion dynamics via the causal consistency of STAR-based generation.
- **Partial Update (PU):** This mechanism prevents updates in pruned regions, confining transformer refinement exclusively to non-converged tokens. Restricting refinement to these active areas eliminates redundant processing while safeguarding the structural integrity of the cumulative feature map.

Experimental results on InfinityStar demonstrate that FastSTAR achieves an end-to-end speedup up to **2.01** \times on a single NVIDIA H100 GPU while maintaining a high PSNR of 28.29. With less than 1% performance degradation, FastSTAR establishes a new Pareto frontier in Text-to-Video generation, consistently outperforming existing acceleration methods as shown in Fig. 2(b). By delivering robust gains across Image-to-Video and Video-to-Video tasks without any additional fine-tuning, our approach provides a practical, scalable solution for state-of-the-art autoregressive video synthesis.

2 Related Work

Autoregressive Video Generation. Early autoregressive (AR)-based video generators treat synthesis as sequential next-token prediction over discrete visual representations [34, 35, 38], which inherently discards spatial structure by

serializing 3D content into a 1D sequence. To address this, some approaches introduce spatiotemporal-aware positional embeddings [40] or remove vector quantization [39, 45] entirely with spatial set-by-set prediction [8]. Recent research also explores spatiotemporal cubes as a more tightly coupled prediction unit [26]. In parallel, VAR-based models reformulate video synthesis as a coarse-to-fine next-scale prediction [14, 22], achieving synthesis quality comparable to diffusion-based models [15, 36] at a fraction of the inference cost.

Efficient Image Synthesis. A diverse landscape of efficiency-oriented strategies has been established for both VAR-based and diffusion-based frameworks. Within the VAR-based framework, existing approaches reduce computational cost through (i) scale-wise token selection with cached-token restoration (FastVAR [10]), (ii) frequency-aware schemes that skip generation steps [16] and stage-aware schemes that prune or approximate computation in later stages [19], and (iii) low-frequency token exclusion in high-resolution stages while preserving fidelity via anchor tokens (SparseVAR [6]). Other directions improve efficiency without explicitly dropping tokens, such as compressing KV cache in a scale-aware manner [17], or modifying decoding to share computation across candidates [7]. In parallel, diffusion-based image synthesis has developed efficiency techniques: step-reduction via fast solvers [23], as well as runtime optimizations that reduce denoising compute through feature caching [47], similarity-based token pruning [42, 43], and diffusion process-aware token merging [2, 9, 24].

Efficient Video Synthesis. The transition from image to video synthesis significantly amplifies computational demands, necessitating specialized acceleration efforts across both autoregressive and diffusion paradigms. On the AR side, training-free methods exploit spatiotemporal redundancy during sequential decoding [37] or mitigate the growing KV-cache bottleneck via compact cache management [18]. For diffusion-based video synthesis, efficiency has been extensively studied through step-reduction via distillation or consistency training [21, 33, 41], as well as optimizations including feature caching across denoising steps [25, 46], token-level reduction via asymmetric attention pruning [30] and cross-frame token merging [20], and pruning of redundant temporal attention [29]. Despite their effectiveness, existing AR frameworks focus on flat sequential decoding, lacking mechanisms to exploit scale-wise redundancy inherent in STAR-based hierarchical models. Meanwhile, diffusion-centric methods rely on cross-step redundancy within denoising trajectories, a property absent in discrete-index generation, making them not directly transferable.

3 Method

3.1 Preliminary

Visual Autoregressive Modeling. Visual Autoregressive modeling (VAR) reformulates image synthesis as a next-scale prediction task. Within this framework, generation is performed through a hierarchy of discrete token maps r_1, r_2, \dots, r_K with progressively increasing resolutions (h_k, w_k) . Each token map r_k at

a given scale follows a joint probability distribution conditioned on the results of all preceding scales:

$$p(r_1, \dots, r_K) = \prod_{k=1}^K p(r_k \mid r_1, \dots, r_{k-1}) \quad (1)$$

This hierarchical structure enables the model to establish global context at lower scales and refine intricate details at higher resolutions.

Spatiotemporal Pyramid Modeling. Following recent spacetime autoregressive frameworks, a video is decomposed into N sequential clips $\{c_1, c_2, \dots, c_N\}$. The initial clip c_1 (at $T = 1$) encodes static appearance cues and establishes the spatiotemporal foundation for the sequence. Subsequent clips where $T > 1$ are modeled as 3D volume pyramid with dimensions (T, h_k, w_k) and are generated:

$$p(c_1, \dots, c_N) = \prod_{c=1}^N \prod_{k=1}^K p(r_k^c \mid r_1^1, \dots, r_{k-1}^c, \psi(t)) \quad (2)$$

where $\psi(t)$ represents the text conditioning.

Residual Feature Accumulation. At each scale k , the transformer predicts a distribution over tokens which is then quantized to produce the discrete token map r_k . This token map represents the residual information needed to refine the video at the current resolution. The feature map f_k is updated by integrating the interpolated results of the current token map r_k with the feature state from the previous scale f_{k-1} via element-wise addition:

$$f_k = \text{Interpolate}(r_k, (h_K, w_K)) + f_{k-1} \quad (3)$$

This recursive relationship ensures that f_k encapsulates the integrated information from all preceding scales, providing a stable foundation for further refinement. To further enhance quality, certain scales repeat this process multiple times at the same resolution before advancing to the next scale. The accumulated feature map is downsampled to the next scale resolution (h_{k+1}, w_{k+1}) :

$$r_{k+1} = \text{Interpolate}(f_k, (h_{k+1}, w_{k+1})) \quad (4)$$

The resulting token map r_{k+1} then functions as the primary input for the transformer block at the subsequent scale $k + 1$.

3.2 Motivation

This work presents an acceleration framework for STAR-based video synthesis by exploiting the scale-wise information redundancy inherent in hierarchical video feature maps. Specifically, we characterize the model through the spectral convergence of information across resolutions, the spatiotemporal duality of feature maps, and the structural justification for prioritizing token pruning over merging in the context of cumulative refinement.

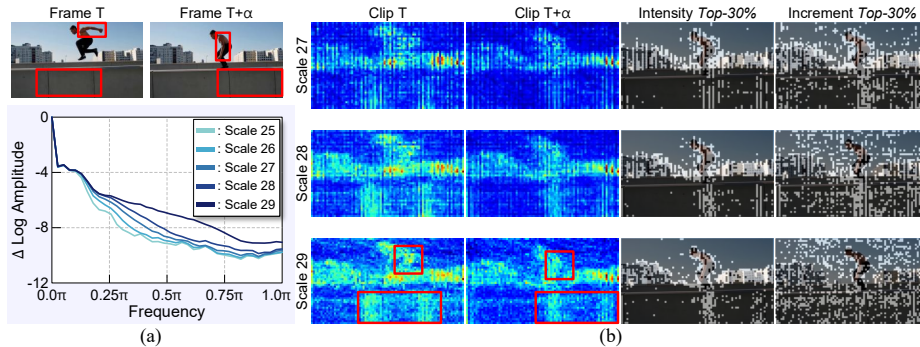


Fig. 4: (a) Scale-wise Fourier-based spectral analysis demonstrates early low-frequency convergence alongside sustained high-frequency updates. (b) High-frequency energy maps show intense localization. Comparing high-intensity locations with large incremental updates reveals significant opportunities for token pruning in converged regions.

Observation 1: Spectral Convergence of Video Feature Maps. Scale-specific information density in the STAR-based video generation pipeline reveals non-uniform distribution across tokens and scales. As demonstrated by the Fourier-based spectral analysis in Fig. 4(a), low-frequency components representing the global structural sketch reach convergence early, exhibiting minimal variance across subsequent late scales. In contrast, high-frequency details, such as moving objects and sharp boundaries, are continuously updated until the final scale. This phenomenon is further substantiated in Fig. 4(b), which presents heatmaps generated by applying an Inverse Fourier Transform (IFT) exclusive to the high-frequency coefficients. These visualizations confirm that high-frequency energy is intensely localized on salient regions, such as human silhouettes and critical background textures. In contrast, the residual increments between successive scales exhibit a scattered, patternless distribution across the entire region. This discrepancy indicates that numerical updates in low-frequency areas fail to emerge as meaningful high-frequency refinements, instead representing redundant computations. Consequently, this localized stability offers a significant opportunity to prune converged regions, concentrating computation on high-frequency areas.

Observation 2: Spatiotemporal Duality of Video Feature Maps. Unlike static images, tokens in the STAR-based framework embody a fundamental spatiotemporal duality, acting as integrated carriers within the accumulated feature map to simultaneously represent motion evolution and decomposed visual textures. As illustrated in Fig. 4(b), high-frequency tokens are not limited to static spatial regions but are densely distributed along motion trajectories—including both the dynamic paths of subjects and the shifting boundaries of the structure. This signifies that the high-frequency energy effectively encodes the temporal continuity required to decode fluid motion and evolving scene geometry. Consequently, redundancy in STAR is fundamentally distinct from that in static image models, necessitating a pruning criterion that transcends simple spatial impor-

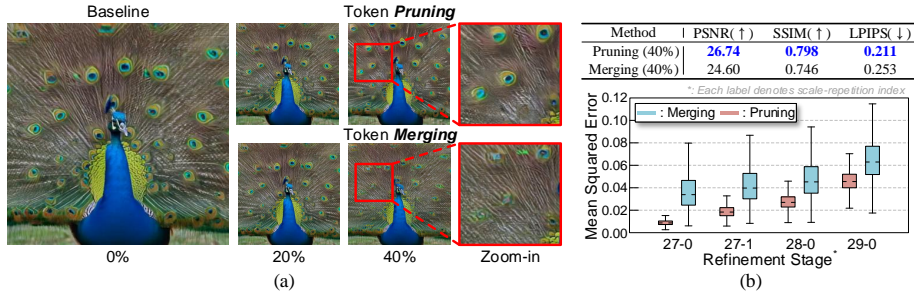


Fig. 5: Comparison of token pruning and merging. (a) Token merging at 40% obliterates high-frequency textures, while pruning preserves fine details even at high compression. (b) Merging exhibits higher average MSE and expanding variance across resolution scales, whereas pruning maintains tighter error bounds.

tance. Integrating both spatial and temporal characteristics is therefore essential to identify tokens that require active updates while bypassing those that have already reached spatiotemporal convergence.

Observation 3: Structural Compatibility of Pruning over Merging. As the STAR-based framework accumulates discrete features through quantization, conventional token merging faces fundamental structural limitations. Averaging similar tokens distorts discrete latent representations, triggering an error feedback loop that spreads spatially as resolution increases. This structural incompatibility is empirically evident in Fig. 5(a), where a 40% merging ratio obliterates high-frequency patterns. In contrast, pruning—which preserves the spatial integrity of randomly selected locations from the initial scale—effectively maintains fine textures. Quantitative analysis in Fig. 5(b) further shows that while both methods exhibit rising Mean Squared Error (MSE) with resolution, merging suffers from a significantly higher average MSE and rapidly expanding variance. Conversely, pruning maintains a much tighter variance even at final scales, demonstrating its superior ability to suppress error propagation. By preserving the spatial integrity of selected tokens, pruning ensures a consistent path for residual updates, preventing the representation drift inherent in merging.

3.3 Spatiotemporal Similarity-based Token Pruning and Partial Update

Building on the observed spectral convergence and spatiotemporal duality of video feature maps, we implement spatiotemporal similarity-based token pruning and a corresponding partial update mechanism to minimize redundant computations within the STAR transformer backbone. This process ensures that only the most informative regions of the video feature map are refined while preserving the structural integrity of already converged regions.

Spatiotemporal Token Pruning (STTP). To identify tokens that exhibit persistent high-frequency energy and require continuous updates, we introduce a pruning methodology based on two distinct similarity metrics derived directly

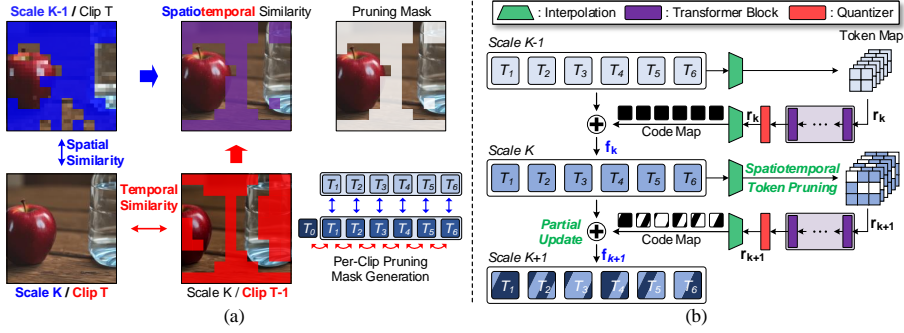


Fig. 6: Overview of Spatiotemporal Token Pruning (STTP) and Partial Update (PU). (a) Spatial similarity and temporal similarity are fused into a unified spatiotemporal score to generate a per-clip pruning mask. (b) Only high-priority tokens are passed through the transformer and quantize at each scale, while unselected regions are filled with zeros via Partial Update to preserve the integrity of the cumulative feature map.

from the video feature maps. These metrics allow us to pinpoint regions of high informational gain with minimal computational overhead. Our strategy employs the inherent structural and motion-related information within the feature maps to guide the pruning process:

- **Spatial Similarity:** To detect spatial refinements across scales, we compute the cosine similarity between feature maps of the previous and current scales:

$$s_{t,k}^{\text{spatial}} = \frac{f_{t,k-1} \cdot f_{t,k}}{\|f_{t,k-1}\| \|f_{t,k}\|}, \quad t = 1, \dots, T \quad (5)$$

As illustrated in Fig. 7, lower similarity scores are intensely localized on salient objects and detailed textures, indicating that these high-frequency regions undergo substantive updates to enhance visual fidelity. This allow us to identify non-converged tokens requiring further refinement while preserving already converged areas.

- **Temporal Similarity:** To exploit temporal continuity within the video feature map, we compute the cosine similarity between the feature maps of clip t and its predecessor $t - 1$:

$$s_{t,k}^{\text{temporal}} = \frac{f_{t-1,k} \cdot f_{t,k}}{\|f_{t-1,k}\| \|f_{t,k}\|}, \quad t = 1, \dots, T \quad (6)$$

As illustrated in Fig. 7, lower similarity scores are concentrated along motion trajectories, identifying regions that require temporal information to represent fluid motion. For the initial clip $f_{1,k}$, temporal importance is determined by comparing with the last scale feature map of the first clip $f_{0,K}$.

Joint Metric Fusion via ℓ_p -norm Dissimilarity. To robustly integrate these indicators into a unified score, we transform the cosine similarity values into a dissimilarity-based importance metric; lower similarity signifies a higher refinement priority. The fusion is defined as a ℓ_p -norm over the two dissimilarity terms:

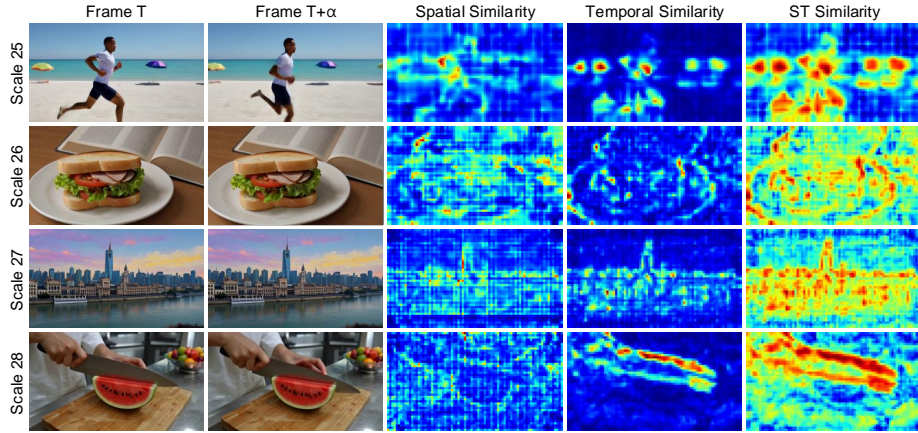


Fig. 7: Visualization of similarity maps across scales and frames. Warmer colors (red) indicate **low similarity**, corresponding to dynamic or high-frequency regions requiring update, while cooler colors (blue) indicate **high similarity** in converged, static regions.

$$\text{Score}_{ST} = [(1 - s_{\text{spatial}})^p + (1 - s_{\text{temporal}})^p]^{1/p} \quad (7)$$

where p modulates the sensitivity to high-dissimilarity regions, higher values of p effectively prioritize tokens that exhibit significant change in *either* the spatial or temporal domain, acting as a soft-maximum operator. Conversely, lower values of p provide a more balanced integration of both terms. We empirically validate the choice of p through ablation studies in § 4.5, and set $p = 2$ for all experiments.

Implementation of Partial Update (PU). To ensure the pruning mask $M \in \{0, 1\}^{h_K \times w_K}$ is compatible with the hierarchical structure of VAR, we downsample the generated pruning mask to match the current token map dimensions (h_k, w_k) via interpolation. The pruning process for the input token map r_k is defined as follows:

$$\hat{r}_k = r_k \odot \text{Interpolate}(M, (h_k, w_k)) \quad (8)$$

The transformer backbone subsequently processes only the selected tokens \hat{r}_k , significantly reducing the computational overhead. After the transformer iterations and quantization are complete, the resulting residual code map is up-sampled back to the video feature map resolution (h_K, w_K) . To maintain the structural integrity of the cumulative VAR process, we implement a partial update strategy. The unselected regions in the expanded residual map are explicitly filled with zeros using the original pruning mask M before being integrated into the previous video feature map f_{k-1} . The partial update for the video feature map f_k is formulated as:

$$f_k = \text{Interpolate}(\hat{r}_k, (h_K, w_K)) \odot M + f_{k-1} \quad (9)$$

This mechanism prevents uncomputed or stale noise from polluting converged regions, ensuring that computational resources are strictly concentrated on the most dynamic and detailed portions of the video.

4 Experiments

4.1 Experimental Setup

Models and Baselines. We evaluate the proposed FastSTAR using InfinityStar [22] as the backbone. To ensure a comprehensive comparison, we implemented representative training-free token reduction baselines: SparseVAR [6], FastVAR [10], and ToMe [1]. Since these methods were originally designed for text-to-image synthesis or non-autoregressive architectures, we extended them to accommodate the temporal dimension by applying their respective reduction mechanisms across the spatiotemporal pyramid. This ensures a fair and competitive evaluation against established image-based acceleration strategies within the video domain. For all experiments, we maintain the default hyperparameters of the backbone model to ensure consistency.

Metrics. We assess our framework across two primary dimensions: inference efficiency and generation quality.

- **Inference Efficiency:** We measure the practical acceleration of our method on a NVIDIA H100 GPU (80GB). Efficiency metrics include end-to-end inference latency across the text encoder and VAE decoder, and the achieved speedup.
- **Generation Quality:** We utilize the VBench [13] suite, evaluating 5-second videos (81 frames) at 720p resolution across all 16 dimensions using the official VBench prompt set. To ensure a fair comparison, we employ the same rewritten prompts used in the evaluation of InfinityStar. Additionally, we report Peak Signal-to-Noise Ratio (PSNR), Structural Similarity Index Measure (SSIM), and Learned Perceptual Image Patch Similarity (LPIPS) [44] to quantify reconstruction fidelity and perceptual similarity. These metrics are computed on 10 videos sampled per VBench dimension for each task (T2V, I2V, and V2V).

Implementations. For the spatiotemporal similarity-based pruning, we apply STTP to the high-resolution refinement stages, which account for the vast majority of the total inference latency. Specifically, we focus on the final four scales to exploit cross-scale and intra-scale redundancies during the synthesis process, alleviating the computational burden while preserving the established structural layouts. For scales with multiple iterations at the same resolution, pruning is applied to early iterations, reserving the final iteration for full-token refinement.

Table 1: Quantitative and efficiency benchmarking for 720p, 5s (81 frames) Text-to-Video generation. We compare FastSTAR with baselines across quality metrics and inference latency; **best results** are shown in bold and second-best results are underlined; † denotes results using prompt rewriting.

Methods	Config	Inference Efficiency		Quality Metrics			VBench Score (†)		
		Latency (s)	Speedup	PSNR (†)	SSIM (†)	LPIPS (↓)	Quality Score	Semantic Score	Total Score
InfinityStar†	8B, 720p, T2V	81.7	1.00×	-	-	-	84.33	82.11	83.89
	● + SparseVAR	56.9	1.44×	26.59	0.789	0.228	82.70	79.86	82.13
	● + FastVAR	50.7	1.61×	25.00	0.757	0.266	81.20	<u>81.18</u>	81.19
	● + ToMe	46.4	1.76×	26.47	0.790	0.227	81.98	80.10	81.60
	● + FastSTAR	42.6	1.92×	28.30	0.828	0.184	83.71	79.96	<u>82.96</u>
	◆ + FastSTAR	40.6	2.01×	28.29	<u>0.828</u>	0.185	83.59	81.51	83.18

● denotes pruning/merging ratio of scale (26, 27, 28, 29) = (20%, 30%, 50%, 60%). ◆ denotes pruning ratio of scale (26, 27, 28, 29) = (20%, 30%, 40%, 70%)

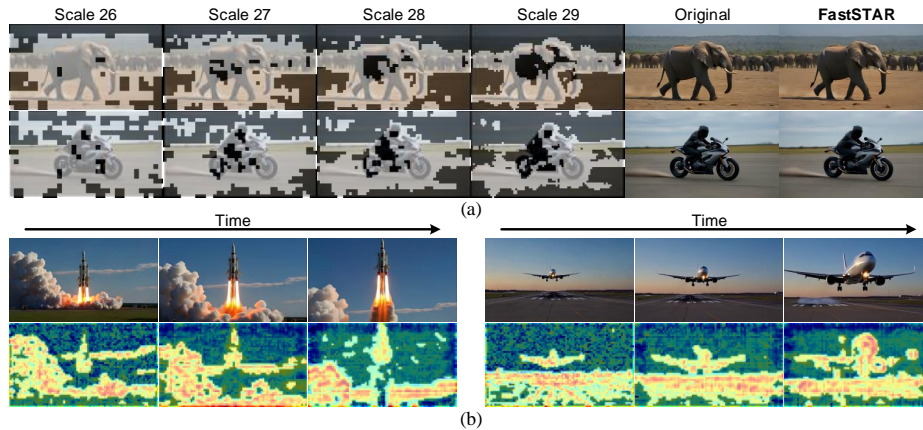


Fig. 8: Qualitative results. (a) Pruning masks across scales and resulting outputs. (b) Frame-level results at the last scale with spatiotemporal similarity heatmaps and pruning masks. **Black** denotes pruned regions and **white** denotes computed regions.

4.2 Comparative Analysis on Text-to-Video Generation

Quantitative Comparison. Table 1 compares the inference efficiency and generation quality of various acceleration schemes applied to the InfinityStar baseline for T2V. Although the base InfinityStar model offers high-fidelity video synthesis, its original inference time of 81.7s imposes a significant computational burden for 720p generation. While existing reduction methods like SparseVAR, FastVAR, and ToMe yield speedups of 1.44×, 1.61×, and 1.76×, respectively, they suffer substantial declines in both VBench scores and Quality Metrics, including PSNR, SSIM, and LPIPS. This degradation stems from their inherent limitations in handling the hierarchical and temporal complexities of STAR. In contrast, FastSTAR maintains high generation quality across different pruning configurations. Specifically, for two configurations with similar pruning ratios—(20%, 30%, 50%, 60%) and (20%, 30%, 40%, 70%)—our method achieves acceleration up to 2.01× with a negligible VBench score reduction of only 0.85%

Table 2: Comparison with state-of-the-art token reduction methods on 720p, 5s (81 frames) Image-to-Video generation; **best results** are shown in bold and **second-best results** are underlined.

Methods	Config	Inference Efficiency		Quality Metrics			VBench Score (↑)		
		Latency (s)	Speedup	PSNR (↑)	SSIM (↑)	LPIPS (↓)	V-I [*] Subject Consistency	V-I ^{**} Bgnd Consistency	Quality Score
InfinityStar	8B, 720p, I2V	81.7	1.00×	-	-	-	97.54	97.37	80.97
	◆ + SparseVAR	55.3	1.56×	23.86	0.754	0.249	96.40	97.05	<u>78.30</u>
	◆ + FastVAR	44.9	1.82×	22.20	0.711	0.292	94.46	95.49	74.83
	◆ + ToMe	52.0	1.57×	<u>23.93</u>	<u>0.757</u>	<u>0.248</u>	<u>96.45</u>	<u>97.06</u>	78.25
	◆ + FastSTAR	40.6	2.01×	25.65	0.809	0.195	97.24	97.29	80.01

◆ denotes pruning ratio of scale (26, 27, 28, 29) = (20%, 30%, 40%, 70%) * : V-I denotes Video-Image ** : Bgnd denotes Background

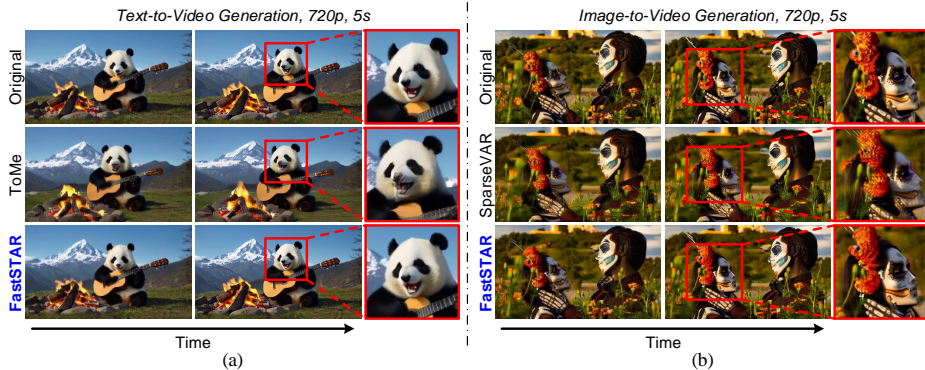


Fig. 9: Qualitative comparison of generation quality. (a) T2V. (b) I2V.

from the baseline. Furthermore, our method significantly outperforms all other baselines in quality metrics, achieving the highest PSNR of 28.29.

Qualitative Comparison. Fig. 8 provides a qualitative visualization of how our STTP accurately identifies redundant regions. As illustrated in Fig. 8(a), as the spatial scale increases, FastSTAR effectively captures areas where further updates are no longer required, spanning both static backgrounds and converged regions within dynamic objects. Furthermore, Fig. 8(b) displays generated video frames overlaid with our fused similarity score heatmaps and the resulting pruning masks. Because temporal characteristics are natively fused into the importance scores, the heatmaps clearly demonstrate that FastSTAR preserves critical motion trajectories while aggressively pruning spatiotemporally redundant tokens, ensuring fluid motion and structural integrity.

4.3 Comparative Analysis on Image-to-Video Synthesis

Quantitative Comparison. We evaluate the performance of FastSTAR against established token reduction baselines, including SparseVAR, FastVAR, and ToMe, as shown in Table 2. For a fair comparison, we align the pruning and merging ratios at (20%, 30%, 40%, 70%) across the final scales of the 720p I2V task. While all methods achieve speedups, FastSTAR significantly outperforms the baselines in maintaining quality metrics, reporting superior scores in PSNR of 25.65.

Table 3: Performance across 480p STAR-based synthesis tasks (T2V, I2V, V2V).

Methods	Config			Inference Efficiency		Quality Metrics		
	Task	Resolution	Frames	Latency (s)	Speedup	PSNR (\uparrow)	SSIM (\uparrow)	LPIPS (\downarrow)
InfinityStar ■ + FastSTAR	<i>Text-to-Video</i>	480p	81	38.3	1.00×	-	-	-
				26.1	1.47×	22.96	0.697	0.262
	<i>Image-to-Video</i>	480p	81	38.0	1.00×	-	-	-
				25.9	1.47×	23.86	0.750	0.234
	<i>Video-to-Video</i>	480p	81	140.2	1.00×	-	-	-
				101.1	1.39×	24.93	0.767	0.219

■ denotes pruning ratio of scale (24, 25, 26, 27) = (20%, 30%, 40%, 70%)

Qualitative Comparison. Fig. 9 compares the generation quality across different tasks and acceleration methods. As illustrated in the T2V task in Fig. 9(a), FastSTAR maintains nearly identical visual quality to the original baseline, preserving intricate textures and structural details that are significantly degraded in ToMe. Similarly, Fig. 9(b) demonstrates that in the I2V task, FastSTAR effectively avoids the severe artifacts and loss of semantic clarity seen in SparseVAR. By accurately identifying redundant regions through spatiotemporal awareness, FastSTAR ensures superior structural integrity and visual consistency, even under the aggressive pruning ratios required for $2.01\times$ acceleration.

4.4 Robustness Across Various Synthesis Tasks

To demonstrate the versatility of our framework, we apply FastSTAR to various synthesis tasks at 480p resolution, including T2V, I2V, and V2V. As summarized in Table 3, our method consistently achieves acceleration across all these tasks while maintaining high reconstruction fidelity. Notably, the acceleration gain at 480p is slightly lower than at 720p due to the reduced scale count and smaller token map dimensions. These results confirm robustness across different conditioning signals and resolutions.

4.5 Ablation Studies

Different Pruning Ratios. The pruning ratio dictates the balance between computational efficiency and generation quality. As shown in Fig. 10(a), increasing the pruning ratio in the final scales results in a direct reduction in runtime, albeit with an expected trade-off in reconstruction fidelity. Through our analysis across scales 26, 27, and 28, we observe that configurations of (20%, 30%, 40%) maintain a stable quality-to-speed slope. Specifically, for the final scale (scale 29), we find that quality remains robust up to a 70% pruning ratio; however, exceeding this threshold leads to severe quality degradation. Consequently, we adopt the (20%, 30%, 40%, 70%) configuration as our primary setting to maximize speedup while preserving structural integrity.

Norm Degree. To analyze the sensitivity of our spatiotemporal score fusion to the choice of norm degree p , we compare $p \in \{1, 2, \infty\}$ in Fig. 10(b). As shown, while all choices yield competitive results, $p = 2$ achieves the best perceptual

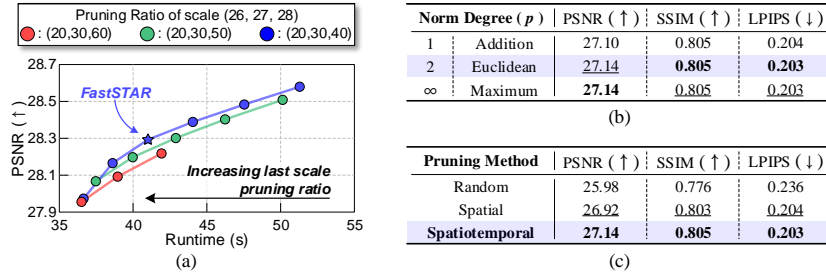


Fig. 10: Ablation studies of FastSTAR. (a) Effect of pruning ratios on runtime and PSNR. (b) Sensitivity to norm degree p in score fusion. (c) Comparison of pruning methods. **Best results** are shown in bold and second-best results are underlined.

quality, recording the highest SSIM and lowest LPIPS. This aligns with its role as a balanced integrator between the maximum behavior of $p = \infty$ and the uniform weighting of $p = 1$, and is therefore adopted as our default configuration.

Pruning Method. To justify the necessity of our spatiotemporal approach, we compare its performance against random and purely spatial-based pruning strategies in Fig. 10(c). Random pruning fails to preserve critical information, resulting in poor quality across all dimensions. While spatial-only pruning offers an improvement, it lacks the temporal context required to maintain fluid motion and consistency. FastSTAR surpasses both baselines across the entire spectrum of metrics, establishing that integrating temporal dynamics into the pruning method is essential for high-fidelity video synthesis.

5 Conclusion

In this work, we presented FastSTAR, a training-free acceleration framework specifically designed for high-quality video generation within the Spacetime AutoRegressive modeling (STAR). Our core innovation, Spatiotemporal Token Pruning (STTP), addresses the "token explosion" at final refinement scales by integrating spatial structural convergence and temporal motion trajectories to identify high-priority tokens. Unlike conventional merging strategies that distort discrete feature distributions, our pruning-over-merging approach, combined with a Partial Update (PU) mechanism, effectively prevents error propagation while bypassing redundant computations.

Experimental results on the InfinityStar model demonstrate that FastSTAR achieves a significant end-to-end speedup of up to $2.01\times$ on a single NVIDIA H100 GPU for 720p video synthesis. Remarkably, this acceleration is achieved with a negligible VBench score degradation of less than 1%, consistently delivering robust performance across various generation modes including T2V, I2V, and V2V. By defining a new Pareto frontier for efficient video synthesis, FastSTAR provides a practical and scalable solution for high-resolution autoregressive modeling in real-world applications.

References

1. Bolya, D., Fu, C.Y., Dai, X., Zhang, P., Feichtenhofer, C., Hoffman, J.: Token merging: Your vit but faster (2023), <https://arxiv.org/abs/2210.09461>
2. Bolya, D., Hoffman, J.: Token merging for fast stable diffusion. In: Proceedings of the IEEE/CVF Conference on Computer Vision and Pattern Recognition (CVPR) Workshops. pp. 4599–4603 (June 2023)
3. Chen, J., Ge, C., Xie, E., Wu, Y., Yao, L., Ren, X., Wang, Z., Luo, P., Lu, H., Li, Z.: Pixart- σ : Weak-to-strong training of diffusion transformer for 4k text-to-image generation (2024), <https://arxiv.org/abs/2403.04692>
4. Chen, J., Wu, Y., Luo, S., Xie, E., Paul, S., Luo, P., Zhao, H., Li, Z.: Pixart- δ : Fast and controllable image generation with latent consistency models (2024), <https://arxiv.org/abs/2401.05252>
5. Chen, J., Yu, J., Ge, C., Yao, L., Xie, E., Wu, Y., Wang, Z., Kwok, J., Luo, P., Lu, H., Li, Z.: Pixart- α : Fast training of diffusion transformer for photorealistic text-to-image synthesis (2023), <https://arxiv.org/abs/2310.00426>
6. Chen, Z., Fan, J., Yu, Z., Zhuang, B., Tan, M.: Frequency-aware autoregressive modeling for efficient high-resolution image synthesis (2025), <https://arxiv.org/abs/2507.20454>
7. Chen, Z., Ma, X., Fang, G., Wang, X.: Collaborative decoding makes visual autoregressive modeling efficient. In: Proceedings of the IEEE/CVF Conference on Computer Vision and Pattern Recognition (CVPR). pp. 23334–23344 (June 2025)
8. Deng, H., Pan, T., Diao, H., Luo, Z., Cui, Y., Lu, H., Shan, S., Qi, Y., Wang, X.: Autoregressive video generation without vector quantization (2025), <https://arxiv.org/abs/2412.14169>
9. Fang, H., Tang, S., Cao, J., Zhang, E., Tang, F., Lee, T.Y.: Attend to not attended: Structure-then-detail token merging for post-training dit acceleration. In: Proceedings of the IEEE/CVF Conference on Computer Vision and Pattern Recognition (CVPR). pp. 18083–18092 (June 2025)
10. Guo, H., Li, Y., Zhang, T., Wang, J., Dai, T., Xia, S.T., Benini, L.: Fastvar: Linear visual autoregressive modeling via cached token pruning. In: Proceedings of the IEEE/CVF International Conference on Computer Vision (ICCV). pp. 19011–19021 (October 2025)
11. Han, J., Liu, J., Jiang, Y., Yan, B., Zhang, Y., Yuan, Z., Peng, B., Liu, X.: Infinity: Scaling bitwise autoregressive modeling for high-resolution image synthesis. In: Proceedings of the IEEE/CVF Conference on Computer Vision and Pattern Recognition (CVPR). pp. 15733–15744 (June 2025)
12. Ho, J., Jain, A., Abbeel, P.: Denoising diffusion probabilistic models (2020), <https://arxiv.org/abs/2006.11239>
13. Huang, Z., He, Y., Yu, J., Zhang, F., Si, C., Jiang, Y., Zhang, Y., Wu, T., Jin, Q., Chanpaisit, N., Wang, Y., Chen, X., Wang, L., Lin, D., Qiao, Y., Liu, Z.: Vbench: Comprehensive benchmark suite for video generative models (2023), <https://arxiv.org/abs/2311.17982>
14. Ji, L., Liu, X., Shang, J., Wang, S., Sun, Y., Wu, H., Wang, H.: Videoar: Autoregressive video generation via next-frame & scale prediction (2026), <https://arxiv.org/abs/2601.05966>
15. Kong, W., Tian, Q., Zhang, Z., Min, R., Dai, Z., Zhou, J., Xiong, J., Li, X., Wu, B., Zhang, J., Wu, K., Lin, Q., Yuan, J., Long, Y., Wang, A., Wang, A., Li, C., Huang, D., Yang, F., Tan, H., Wang, H., Song, J., Bai, J., Wu, J., Xue, J., Wang, J., Wang, K., Liu, M., Li, P., Li, S., Wang, W., Yu, W., Deng, X., Li, Y., Chen,

- Y., Cui, Y., Peng, Y., Yu, Z., He, Z., Xu, Z., Zhou, Z., Xu, Z., Tao, Y., Lu, Q., Liu, S., Zhou, D., Wang, H., Yang, Y., Wang, D., Liu, Y., Jiang, J., Zhong, C.: Hunyuanvideo: A systematic framework for large video generative models (2025), <https://arxiv.org/abs/2412.03603>
16. Li, J., Ma, Y., Zhang, X., Wei, Q., Liu, S., Zhang, L.: Skipvar: Accelerating visual autoregressive modeling via adaptive frequency-aware skipping (2025), <https://arxiv.org/abs/2506.08908>
 17. Li, K., Chen, Z., Yang, C.Y., Hwang, J.N.: Memory-efficient visual autoregressive modeling with scale-aware kv cache compression (2025), <https://arxiv.org/abs/2505.19602>
 18. Li, K., Shah, M., Shang, Y.: Packcache: A training-free acceleration method for unified autoregressive video generation via compact kv-cache (2026), <https://arxiv.org/abs/2601.04359>
 19. Li, S., Wang, K., Khan, S., Khan, F.S., Yang, J., Wang, Y.: Stagevar: Stage-aware acceleration for visual autoregressive models (2025), <https://arxiv.org/abs/2512.16483>
 20. Li, X., Ma, C., Yang, X., Yang, M.H.: Vidtome: Video token merging for zero-shot video editing. In: Proceedings of the IEEE/CVF Conference on Computer Vision and Pattern Recognition (CVPR). pp. 7486–7495 (June 2024)
 21. Lin, S., Yang, X.: Animatediff-lightning: Cross-model diffusion distillation (2024), <https://arxiv.org/abs/2403.12706>
 22. Liu, J., Han, J., Yan, B., Wu, H., Zhu, F., Wang, X., Jiang, Y., Peng, B., Yuan, Z.: Infinitystar: Unified spacetime autoregressive modeling for visual generation (2025), <https://arxiv.org/abs/2511.04675>
 23. Lu, C., Zhou, Y., Bao, F., Chen, J., LI, C., Zhu, J.: Dpm-solver: A fast ode solver for diffusion probabilistic model sampling in around 10 steps. In: Koyejo, S., Mohamed, S., Agarwal, A., Belgrave, D., Cho, K., Oh, A. (eds.) Advances in Neural Information Processing Systems. vol. 35, pp. 5775–5787. Curran Associates, Inc. (2022), https://proceedings.neurips.cc/paper_files/paper/2022/file/260a14acce2a89dad36adc8eefe7c59e-Paper-Conference.pdf
 24. Lu, W., Zheng, S., Xia, Y., Wang, S.: Toma: Token merge with attention for diffusion models (2025), <https://arxiv.org/abs/2509.10918>
 25. Lv, Z., Si, C., Song, J., Yang, Z., Qiao, Y., Liu, Z., Wong, K.Y.K.: Fastercache: Training-free video diffusion model acceleration with high quality (2025), <https://arxiv.org/abs/2410.19355>
 26. Ren, S., Chen, C., Wang, Z., Song, L., Zhu, X., Yuille, A., Yang, Y., Lu, J.: Autoregressive video generation beyond next frames prediction (2025), <https://arxiv.org/abs/2509.24081>
 27. Rombach, R., Blattmann, A., Lorenz, D., Esser, P., Ommer, B.: High-resolution image synthesis with latent diffusion models (2022), <https://arxiv.org/abs/2112.10752>
 28. Song, J., Meng, C., Ermon, S.: Denoising diffusion implicit models (2022), <https://arxiv.org/abs/2010.02502>
 29. Su, S., Liu, J., Gao, L., Song, J.: F³-pruning: A training-free and generalized pruning strategy towards faster and finer text-to-video synthesis. Proceedings of the AAAI Conference on Artificial Intelligence **38**(5), 4961–4969 (Mar 2024). <https://doi.org/10.1609/aaai.v38i5.28300>, <https://ojs.aaai.org/index.php/AAAI/article/view/28300>
 30. Sun, W., Tu, R.C., Liao, J., Jin, Z., Tao, D.: Asymrn: Video diffusion transformers acceleration with asymmetric reduction and restoration. In: International Conference on Machine Learning. pp. 57694–57711. PMLR (2025)

31. Tian, K., Jiang, Y., Yuan, Z., Peng, B., Wang, L.: Visual autoregressive modeling: Scalable image generation via next-scale prediction. In: Globerson, A., Mackey, L., Belgrave, D., Fan, A., Paquet, U., Tomczak, J., Zhang, C. (eds.) *Advances in Neural Information Processing Systems*. vol. 37, pp. 84839–84865. Curran Associates, Inc. (2024). <https://doi.org/10.52202/079017-2694>, https://proceedings.neurips.cc/paper_files/paper/2024/file/9a24e284b187f662681440ba15c416fb-Paper-Conference.pdf
32. Wan, T., Wang, A., Ai, B., Wen, B., Mao, C., Xie, C.W., Chen, D., Yu, F., Zhao, H., Yang, J., Zeng, J., Wang, J., Zhang, J., Zhou, J., Wang, J., Chen, J., Zhu, K., Zhao, K., Yan, K., Huang, L., Feng, M., Zhang, N., Li, P., Wu, P., Chu, R., Feng, R., Zhang, S., Sun, S., Fang, T., Wang, T., Gui, T., Weng, T., Shen, T., Lin, W., Wang, W., Wang, W., Zhou, W., Wang, W., Shen, W., Yu, W., Shi, X., Huang, X., Xu, X., Kou, Y., Lv, Y., Li, Y., Liu, Y., Wang, Y., Zhang, Y., Huang, Y., Li, Y., Wu, Y., Liu, Y., Pan, Y., Zheng, Y., Hong, Y., Shi, Y., Feng, Y., Jiang, Z., Han, Z., Wu, Z.F., Liu, Z.: Wan: Open and advanced large-scale video generative models (2025), <https://arxiv.org/abs/2503.20314>
33. Wang, X., Zhang, S., Zhang, H., Liu, Y., Zhang, Y., Gao, C., Sang, N.: Videolcm: Video latent consistency model (2023), <https://arxiv.org/abs/2312.09109>
34. Wang, X., Zhang, X., Luo, Z., Sun, Q., Cui, Y., Wang, J., Zhang, F., Wang, Y., Li, Z., Yu, Q., Zhao, Y., Ao, Y., Min, X., Li, T., Wu, B., Zhao, B., Zhang, B., Wang, L., Liu, G., He, Z., Yang, X., Liu, J., Lin, Y., Huang, T., Wang, Z.: Emu3: Next-token prediction is all you need (2024), <https://arxiv.org/abs/2409.18869>
35. Yan, W., Zhang, Y., Abbeel, P., Srinivas, A.: Videogpt: Video generation using vq-vae and transformers (2021), <https://arxiv.org/abs/2104.10157>
36. Yang, Z., Teng, J., Zheng, W., Ding, M., Huang, S., Xu, J., Yang, Y., Hong, W., Zhang, X., Feng, G., Yin, D., Zhang, Y., Wang, W., Cheng, Y., Xu, B., Gu, X., Dong, Y., Tang, J.: Cogvideox: Text-to-video diffusion models with an expert transformer (2025), <https://arxiv.org/abs/2408.06072>
37. Ye, Y., Guo, J., Wu, H., He, T., Pearce, T., Rashid, T., Hofmann, K., Bian, J.: Fast autoregressive video generation with diagonal decoding (2025), <https://arxiv.org/abs/2503.14070>
38. Yu, L., Cheng, Y., Sohn, K., Lezama, J., Zhang, H., Chang, H., Hauptmann, A.G., Yang, M.H., Hao, Y., Essa, I., et al.: Magvit: Masked generative video transformer. In: *2023 IEEE/CVF Conference on Computer Vision and Pattern Recognition (CVPR)*. pp. 10459–10469. IEEE Computer Society (2023)
39. Yu, L., Lezama, J., Gundavarapu, N.B., Versari, L., Sohn, K., Minnen, D., Cheng, Y., Birodkar, V., Gupta, A., Gu, X., Hauptmann, A.G., Gong, B., Yang, M.H., Essa, I., Ross, D.A., Jiang, L.: Language model beats diffusion – tokenizer is key to visual generation (2024), <https://arxiv.org/abs/2310.05737>
40. Yuan, H., Chen, W., Cen, J., Yu, H., Liang, J., Chang, S., Lin, Z., Feng, T., Liu, P., Xing, J., Luo, H., Tang, J., Wang, F., Yang, Y.: Lumos-1: On autoregressive video generation from a unified model perspective (2025), <https://arxiv.org/abs/2507.08801>
41. Zhai, Y., Lin, K., Yang, Z., Li, L., Wang, J., Lin, C.C., Doermann, D., Yuan, J., Wang, L.: Motion consistency model: Accelerating video diffusion with disentangled motion-appearance distillation. In: Globerson, A., Mackey, L., Belgrave, D., Fan, A., Paquet, U., Tomczak, J., Zhang, C. (eds.) *Advances in Neural Information Processing Systems*. vol. 37, pp. 111000–111021. Curran Associates, Inc. (2024). <https://doi.org/10.52202/079017-3524>, <https://proceedings.neurips.cc/>

- paper_files/paper/2024/file/c859b99b5d717c9035e79d43dfd69435-Paper-Conference.pdf
42. Zhang, E., Tang, J., Ning, X., Zhang, L.: Training-free and hardware-friendly acceleration for diffusion models via similarity-based token pruning. In: Proceedings of the AAAI Conference on Artificial Intelligence. vol. 39, pp. 9878–9886 (2025)
 43. Zhang, E., Xiao, B., Tang, J., Ma, Q., Zou, C., Ning, X., Hu, X., Zhang, L.: Token pruning for caching better: 9 times acceleration on stable diffusion for free (2024), <https://arxiv.org/abs/2501.00375>
 44. Zhang, R., Isola, P., Efros, A.A., Shechtman, E., Wang, O.: The unreasonable effectiveness of deep features as a perceptual metric (2018), <https://arxiv.org/abs/1801.03924>
 45. Zhao, Y., Xiong, Y., Krähenbühl, P.: Image and video tokenization with binary spherical quantization (2024), <https://arxiv.org/abs/2406.07548>
 46. Zhou, X., Liang, D., Chen, K., Feng, T., Chen, X., Lin, H., Ding, Y., Tan, F., Zhao, H., Bai, X.: Less is enough: Training-free video diffusion acceleration via runtime-adaptive caching (2025), <https://arxiv.org/abs/2507.02860>
 47. Zou, C., Liu, X., Liu, T., Huang, S., Zhang, L.: Accelerating diffusion transformers with token-wise feature caching (2025), <https://arxiv.org/abs/2410.05317>

Appendix

A Attention Map and Important Tokens.

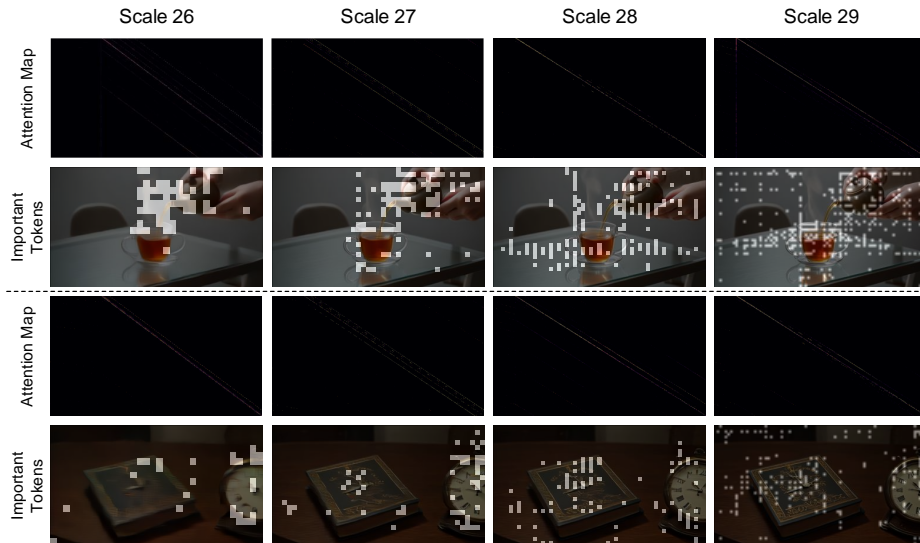


Fig. A.1: Visualization of attention score maps and their corresponding important tokens.

To further justify our pruning strategy, we analyze the relationship between the self-attention mechanism and the regions requiring refinement within the STAR transformer backbone. Specifically, we compute attention score maps by summing the attention scores over the query dimension.

As illustrated in Fig. A.1, these heatmaps exhibit a high degree of sparsity. Notably, the regions with high attention scores strongly align with the non-converged tokens—the areas that still require spatiotemporal updates and textural refinement. This alignment indicates that the self-attention mechanism naturally focuses on parts of the video that are not yet fully converged. By pruning tokens with near-zero attention weights, FastSTAR effectively concentrates computational power on these critical, non-converged regions. This optimization ensures that our spatiotemporal pruning remains consistent with the model’s internal behavior, maintaining high-fidelity synthesis while eliminating redundant computations.

B Profiling the Token Reduction Overhead.

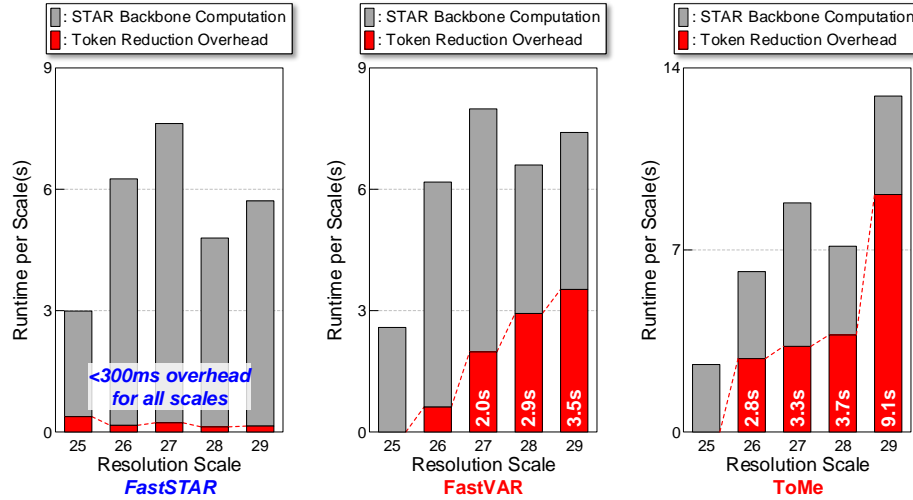


Fig. A.2: Latency breakdown and overhead analysis across different resolution scales.

To empirically validate the minimal overhead of our proposed STTP and PU mechanisms as discussed in § 3.3, we conducted precise latency profiling using NVIDIA Nsight Systems. As illustrated in Fig. A.2, we decomposed the runtime per resolution scale into two components: the STAR Backbone Computation (representing the original InfinityStar execution time) and the Token Reduction Overhead (representing the additional time required by each acceleration scheme). All measurements were recorded after a 30% warmup phase to ensure architectural stability.

The profiling results reveal a critical scalability bottleneck in prior methods. For FastVAR and ToMe, the overhead increases quadratically with the resolution scale, primarily due to layer-wise merging and unmerging operations within the transformer blocks. At the final scale (Scale 29), where the token count reaches 72,000, the overhead for ToMe exceeds 9.1s, significantly diminishing the practical gains from token reduction. In contrast, FastSTAR maintains a near-constant overhead of less than 300ms across all scales, regardless of the token counts. This efficiency stems from our similarity-based pruning strategy, which operates on the fixed, lower-dimensional video feature map rather than the transformer backbone’s expanding token space. FastSTAR ensures that the reduction in backbone computation directly translates into end-to-end acceleration without introducing a new latency bottleneck.

C Inference Efficiency on Another GPU.

Methods	Config	Inference Efficiency		Methods	Config	Inference Efficiency	
		Latency (s)	Speedup			Latency (s)	Speedup
InfinityStar	8B, 720p, T2V	109.7	1.00×	InfinityStar	8B, 720p, I2V	109.7	1.00×
	◆ + SparseVAR	74.7	1.47×		◆ + SparseVAR	70.6	1.55×
	◆ + FastVAR	61.1	1.79×		◆ + FastVAR	61.0	1.80×
	◆ + ToMe	70.9	1.55×		◆ + ToMe	72.8	1.50×
	◆ + FastSTAR	57.5	1.91×		◆ + FastSTAR	57.3	1.91×

◆ denotes pruning ratio of scale (26, 27, 28, 29) = (20%, 30%, 40%, 70%)

Table A.1: Inference efficiency benchmarking on A100 GPU (720p, 5s, 81 frames)

To demonstrate the hardware-agnostic efficiency of our framework, we evaluate the inference performance of FastSTAR on a single NVIDIA A100 GPU (80GB). As summarized in Table. A.1, our method consistently achieves the highest speedup across both T2V and I2V tasks compared to all other baselines.

In the T2V task, FastSTAR delivers a substantial speedup that outperforms established baselines, including SparseVAR, FastVAR, and ToMe. Similarly, in the I2V task, our method maintains a clear lead over existing reduction schemes, establishing the Pareto frontier. These results confirm that the spatiotemporal similarity-based pruning strategy is not limited to specific high-end hardware but delivers robust, consistent acceleration across different GPU architectures.

D Geometric and Statistical Analysis of the Score Fusion.

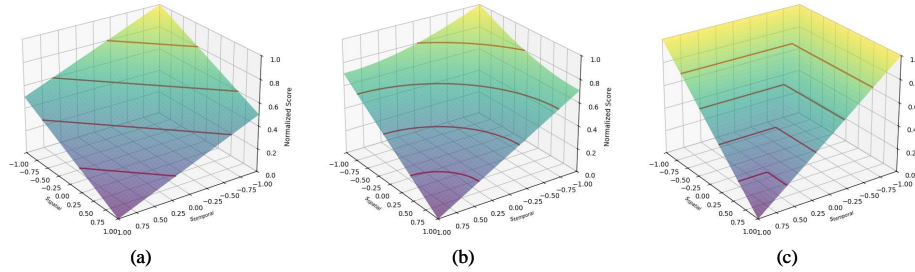


Fig. A.3: 3D landscapes of the spatiotemporal score fusion function, illustrating the fusion geometries for (a) $p = 1$ (Addition), (b) $p = 2$ (Euclidean), and (c) $p = \infty$ (Maximum).

To provide deeper intuition for our ablation study (§ 4.5) on the norm degree $p \in \{1, 2, \infty\}$, Fig. A.3 visualizes the 3D landscapes of our spatial and temporal similarity fusion functions.

- **(a) l_1 -norm ($p = 1$):** Forms a linear, planar surface. It treats both metrics independently with uniform weighting, failing to emphasize tokens that are moderately important in both domains.

- (b) l_2 -norm ($p = 2$): Forms a smooth, convex landscape. This synergistic geometry effectively couples the two dimensions, acting as a *balanced integrator* that smoothly amplifies tokens that exhibit variation across both domains. This corroborates our optimal empirical results of the highest SSIM and the lowest LPIPS.
- (c) **Max norm** ($p = \infty$): Defined by sharp creases, it bounds the score using only the maximum dimension. This ignores the secondary metric entirely, leading to suboptimal feature representation.

These geometries visually demonstrate why our l_2 -norm-based method is the most robust choice for integrating spatiotemporal dynamics while preserving critical high-frequency details.

Score Distribution Analysis. To further illustrate this advantage, Fig. A.4 visualizes the resulting token score distributions across varying resolution scales. The scores generated by l_1 -norm (green) and Max norm (yellow) are highly concentrated within a narrow band. This dense clustering severely limits discriminative power, making it difficult to set clear boundaries during our top- k masking process, as many tokens share near-identical scores. In contrast, our l_2 -norm formulation (purple) produces a significantly broader distribution with a wider dynamic range. This expanded variance smoothly disperses the scores, enabling the top- k selection mechanism to distinctly and robustly separate critical tokens from redundant ones.

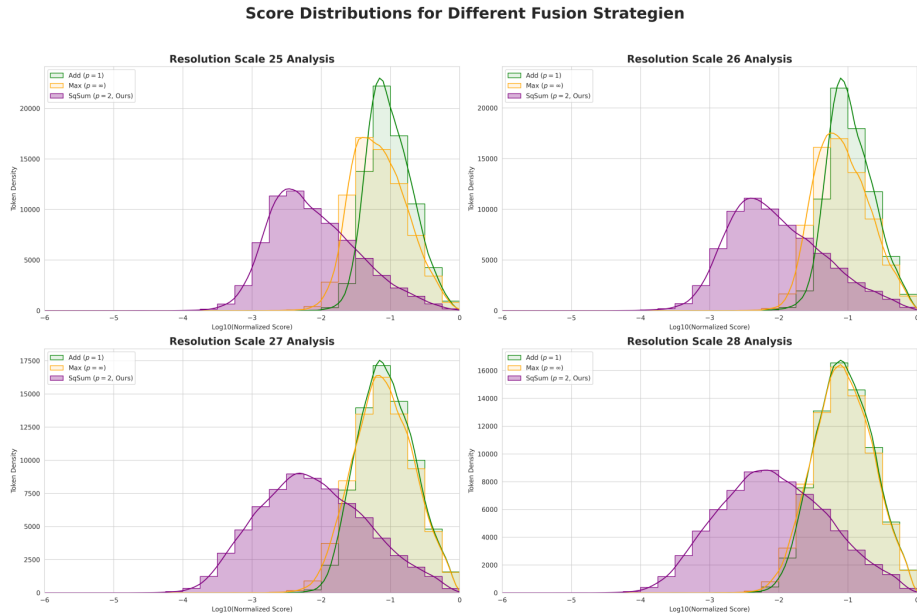


Fig. A.4: Log-scale spatiotemporal score distribution analysis of fusion functions across resolution scales.

E More Quantitative Results.

Methods	Config	VBench Score (↑)							
		Motion Smoothness	Temporal Flickering	Human Action	Object Class	Background Consistency	Subject Consistency	Multiple Object	Color
InfinityStar†	8B, 720p, T2V	98.73	98.45	98.00	96.99	95.83	95.10	87.50	88.92
	● + SparseVAR	98.60	98.52	99.00	78.56	95.13	94.47	86.74	87.47
	● + FastVAR	98.51	98.41	<u>98.50</u>	<u>93.43</u>	94.30	92.69	80.72	87.77
	● + ToMe	98.69	98.59	98.00	79.39	94.97	94.03	83.65	89.26
	● + FastSTAR	<u>98.79</u>	98.58	98.00	81.01	95.66	94.80	85.29	<u>88.49</u>
	◆ + FastSTAR	98.82	<u>98.59</u>	97.50	96.24	<u>95.42</u>	<u>94.76</u>	<u>85.98</u>	87.87

Methods	Config	VBench Score (↑)							
		Spatial Relationship	Dynamic Degree	Imaging Quality	Aesthetic Quality	Scene	Overall Consistency	Temporal Style	Appearance Style
InfinityStar†	8B, 720p, T2V	83.21	70.14	68.00	64.17	53.09	27.72	25.76	20.83
	● + SparseVAR	82.44	59.72	66.34	62.34	52.65	27.74	25.72	21.03
	● + FastVAR	<u>84.27</u>	63.19	62.19	58.84	54.51	27.81	25.73	20.74
	● + ToMe	85.70	52.78	65.41	62.30	<u>53.96</u>	27.73	<u>25.73</u>	20.70
	● + FastSTAR	83.00	65.28	66.92	63.61	53.02	27.76	25.72	20.71
	◆ + FastSTAR	81.51	<u>64.58</u>	<u>66.83</u>	<u>63.58</u>	53.23	<u>27.80</u>	25.76	<u>20.75</u>

● denotes pruning/merging ratio of scale (26, 27, 28, 29) = (20%, 30%, 50%, 60%), ◆ denotes pruning ratio of scale (26, 27, 28, 29) = (20%, 30%, 40%, 70%)

Table A.2: Quantitative and efficiency benchmarking for 720p, 5s (81 frames) Text-to-Video generation. **Best results** are highlighted in bold and second-best results are underlined; † denotes results using prompt rewriting.

As discussed in § 4.2, we provide a comprehensive breakdown of the VBench scores to offer a more granular evaluation of our framework. Table A.2 presents the results across all 16 dimensions of the VBench suite for the 720p, T2V generation task. These scores were obtained under the same experimental settings and evaluation protocols as those detailed in the main manuscript to ensure consistency across all performance metrics. The full report further substantiates the robustness of FastSTAR in maintaining high fidelity across diverse categories, ranging from motion smoothness to appearance style.

F More Qualitative Results.

To provide a more comprehensive evaluation of FastSTAR, we present extended qualitative results across diverse scenarios and configurations. Fig. A.5 offers additional side-by-side comparisons, highlighting our method’s superior ability to preserve fine-grained textures compared to existing baselines. The galleries in Fig. A.6 and Fig. A.7 demonstrate the robust generation capabilities of our framework in 720p Text-to-Video and Image-to-Video tasks, showcasing consistent high-fidelity synthesis across various semantic categories.

Furthermore, Fig. A.8 illustrates the versatility of FastSTAR in 480p resolution tasks, including T2V, I2V, and V2V. These results collectively confirm that our spatiotemporal pruning strategy effectively maintains structural integrity and motion continuity across different resolutions and conditioning signals, producing high-fidelity results from the original while significantly reducing inference latency.

Text-to-Video Generation, 720p, 5s

Original



+ToMe



+FastSTAR



A *young woman*, with gentle features and long, flowing hair, is kneeling down beside a fluffy *golden retriever*. She is ...

Image-to-Video Generation, 720p, 5s

Original



+FastVAR



+FastSTAR



a close-up of a *hippopotamus* eating grass in a field

Fig. A.5: Additional Side-by-Side comparison of FastSTAR with ToMe, FastVAR.

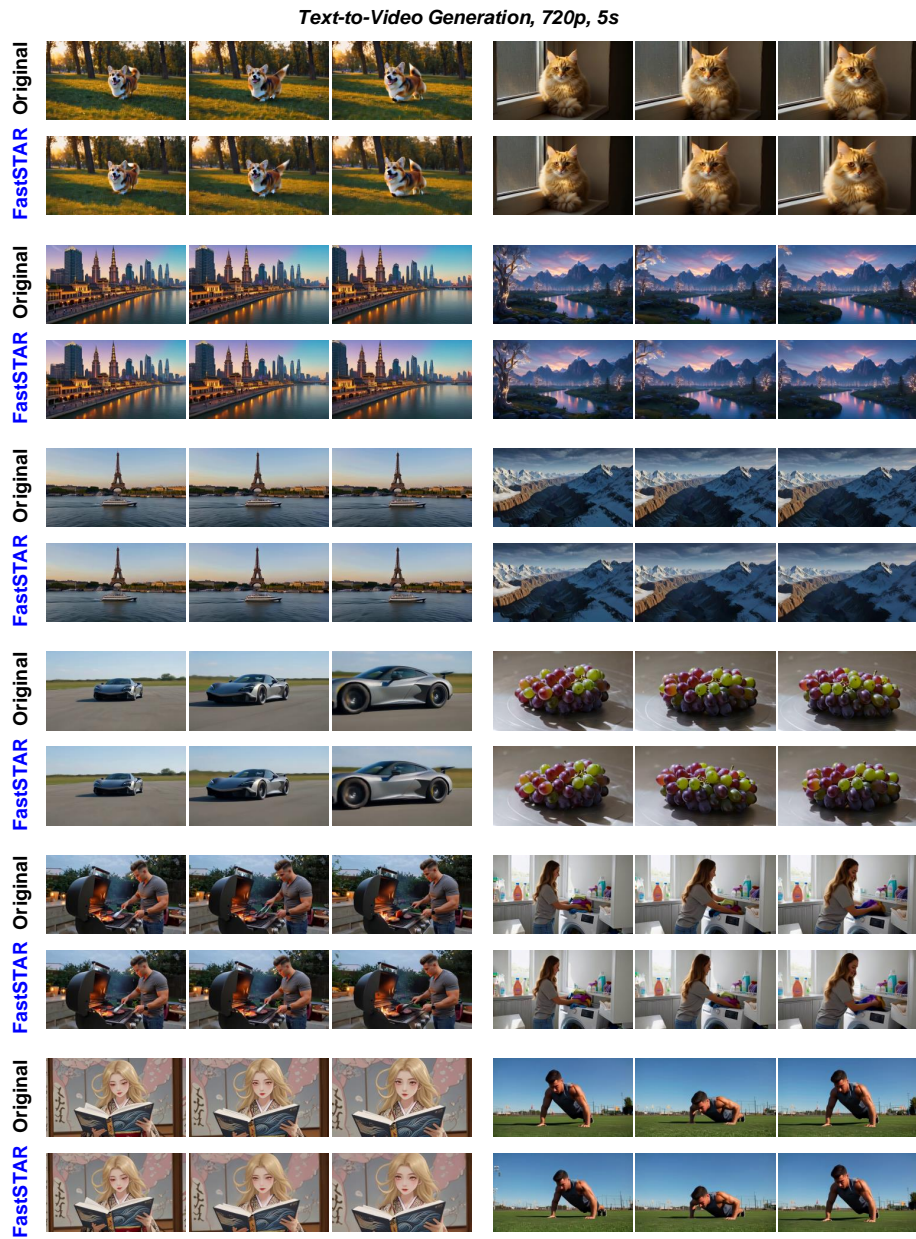


Fig. A.6: Text-to-Video generation results at 720p resolution.

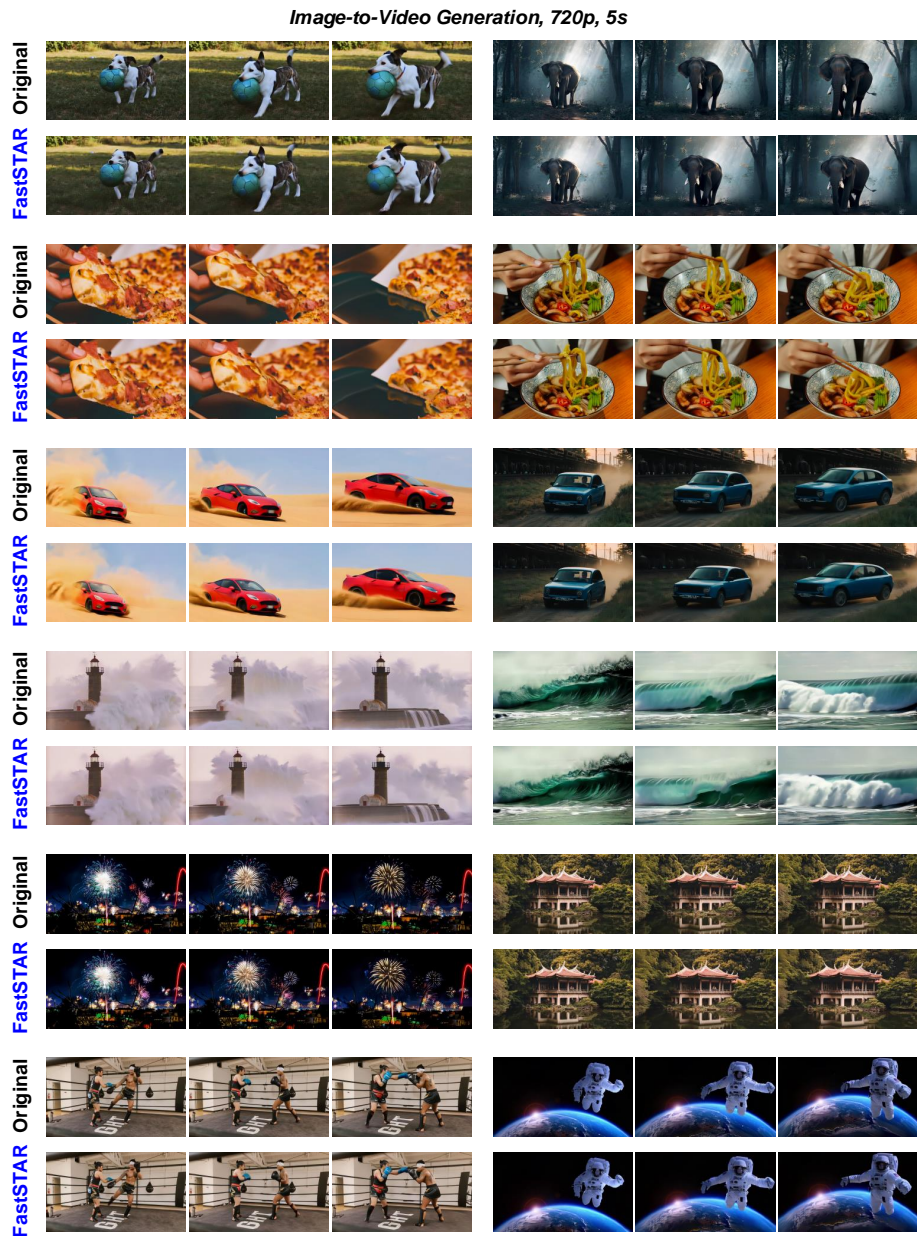


Fig. A.7: Image-to-Video generation results at 720p resolution.

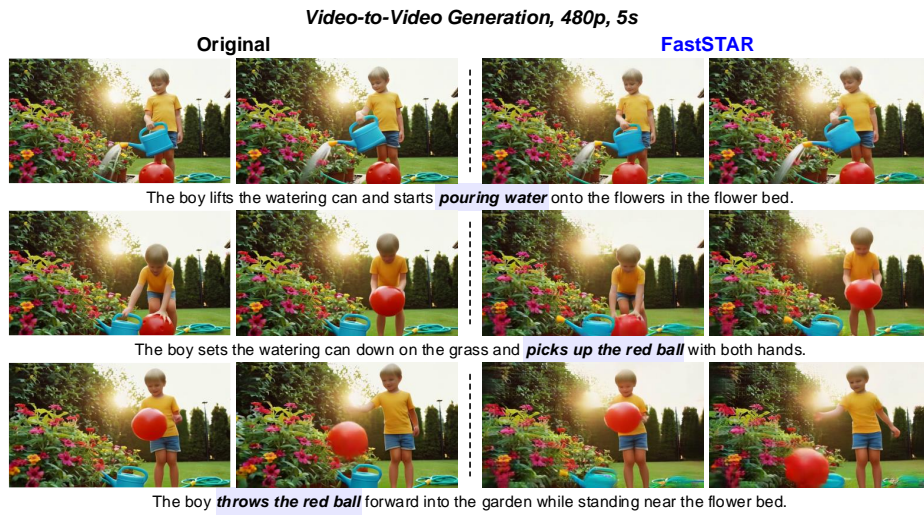
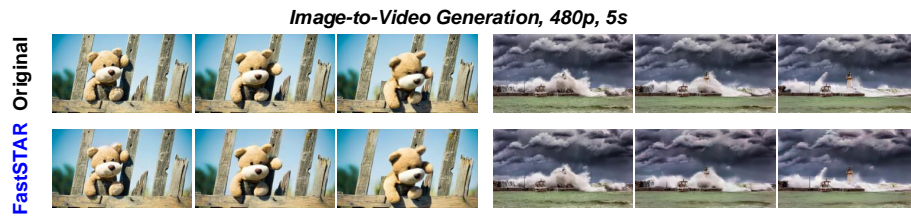


Fig. A.8: Qualitative examples across multiple 480p generation tasks.